Electronic Supplementary Material (ESI) for Physical Chemistry Chemical Physics.

Kinetic energy distributions of atomic ions from disintegration of argon containing nanoclusters in moderately intense nanosecond laser fields:

Coulomb explosion or hydrodynamic expansion

Supplemental Document

Steven Tran,[1] Kim C. Tran,[1] Axel Saenz Rodriguez,[2] and Wei Kong[1]*

1. Department of Chemistry, Oregon State University, Corvallis, Oregon, 97331
2. Department of Mathematics, Oregon State University, Corvallis, Oregon, 97331

Manuscript for submission to the journal of Physical Chemistry Chemical Physics, February 14, 2024

*Corresponding author, 541-737-6714, wei.kong@oregonstate.edu

1. Time-of-flight profiles of atomic ions

An analytical expression of the time-of-flight (TOF) profile $f_m(t)$ for each atomic ion with a

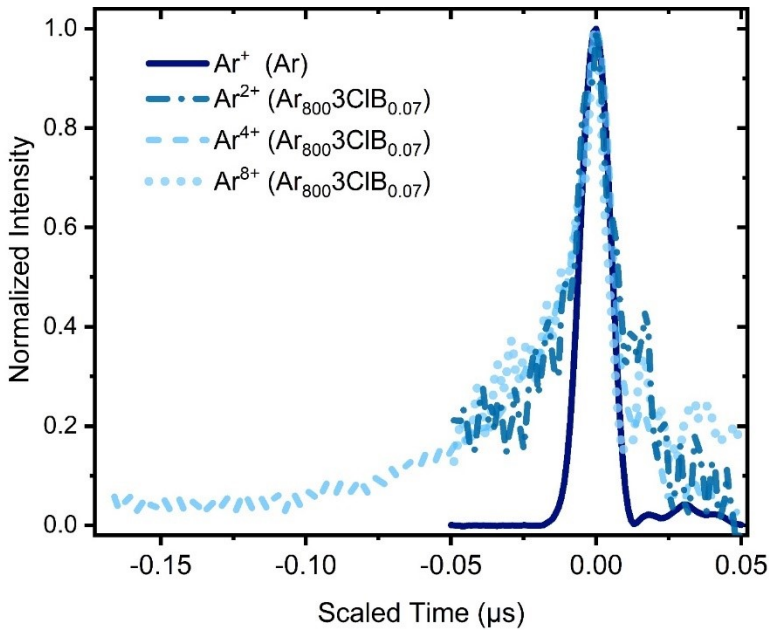

Figure S1: Scaled TOF profiles. The solid blue line represents Ar^+ from a gaseous Ar beam obtained at a stagnation pressure of 1 atm. The dashed/dotted traces represent the TOF profiles of MCAI from the argon cluster $Ar_{800}3ClB_{0.07}$.

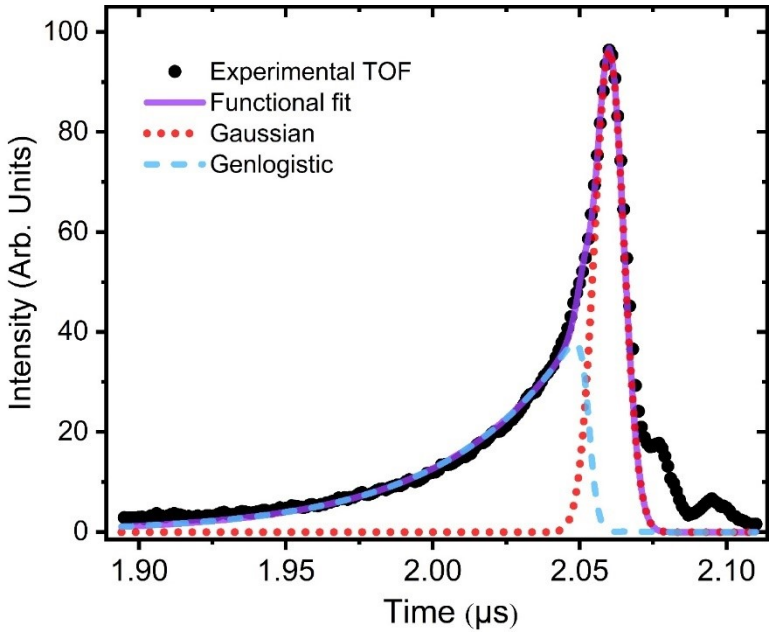

Figure S2: Fitting result of the TOF profile of Ar^{4+} from $^{Ar_{800}3ClB_{0.07}}$ (black dots), including the Gaussian (red dotted line), the Genlogistic function (blue dashed line), and the total fitting result (purple continuous line).

mass-to-charge ratio *m* is necessary to help disentangle the contribution of ion velocity from the noises and detector responses, as explained in the main text. Fig. S1 shows the scaled and recentered TOF profiles of multiply charged atomic ions (MCAI) from $A^{r_{800}3ClB_{0.07}}$ in comparison with the profile of Ar^+ obtained from argon gas. The similarity among these profiles near the peak position suggests that the right side (longer time) of each profile is related to the detector response, and the small peak is most likely due to the oscillation caused by the detector circuit. The rise edge on the left side (shorter time) of each MCAI is related to the limited transmission of high energy ions through the aperture on the extractor. The overall fitting result using Eq. 1 from the main text for Ar^{4+} is shown in Fig. S2. The misfit in the leading edge has an effect in the calculation of the final kinetic energy, and our calculation, with a slightly lower intensity than the experimental result, thus represents a conservative estimate of the average value. In the worst-case scenario, this under-estimate can be a factor of two lower than the value obtained from a fitting with a more complicated fitting function, due to the heavier weight on the high energy tail in the KE calculation. A minor misfit in the overlapping region between the Genlogistic and Gaussian function is unfortunately magnified in the subsequent data processing, particularly for large clusters. Consequently as explained in the main text, the resulting average

speed and energy have large uncertainties and the reported values should be considered as lower limits. Without the glitch caused by the small misfit, the final kinetic energy distribution is Maxwellian, as shown in Fig. 4 and 5 of the main text.

2. Kinetic energy distributions derived from time-of-flight profiles

2.1 From velocity distributions to time-of-flight profiles

Figure S3 shows the definition of variables based on the experimental setup for the following derivation. After a cluster disintegrates, MCAI are accelerated by the extraction field between the Kicker and the Extractor electrodes. Different from Fig. 1 in the main text, this experiment does not include the Retarder, and the Extractor was always grounded, hence in the current treatment, the Extractor and the flight tube are treated as one unit with ground potential. Moreover, the effective area of the MCP detector is 48 mm in diameter, the inner diameter of the flight tube is close to 50 mm, the diameter of the aperture on the Extractor is only 1 mm, and the flight tube is 270 mm. Based on our calculation, if an ion can pass through the aperture, it can reach the effective area of the MCP and it will not collide with the inner wall of the flight tube.

The arrival times (t) of these ions at the detector is related to the projection of their velocity along the flight axis (x-axis), $v_{x'}$ through the following equation:

$$t = t_{acceleration1} + t_{fieldfree} + t_{acceleration2}$$
$$= \frac{2l_0}{v_x + \sqrt{v_x^2 + 2a_0 l_0}} + \frac{l_1}{\sqrt{v_x^2 + 2a_0 l_0}} + \frac{2l_2}{\sqrt{v_x^2 + 2a_0 l_0} + \sqrt{v_x^2 + 2a_0 l_0 + 2a_2 l_2}}, \quad \text{(S1)}$$

where a_0 is the acceleration between the Kicker and the Extractor electrodes, l_0 is the distance of travel in the acceleration region 1, Δ is the aperture radius on the Extractor, l_1 is the length of the flight tube, l_2 is the distance between the flight tube and the microchannel plate detector (acceleration region 2), and a_2 is the acceleration of this region. Eq. S1 shows that the time-of-flight for each region is given by the length of the region divided by the average velocity between

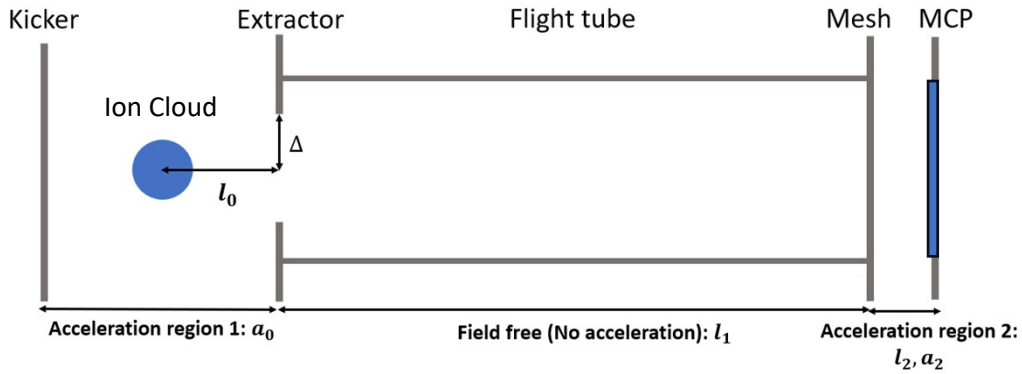

Figure S3: Definitions of variables based on the experimental setup. The blue patch on the MCP represents its effective area (48 mm in diameter)

the initial and final velocity in the region.

If we assume that the MCAI are produced with an isotropic angular distribution $P_m(v_x,v_y,v_z)$, we may write

$$P_m(v_x,v_y,v_z) = \frac{F_m(v)}{4\pi v^2} \quad , \tag{S2}$$

where $v = \sqrt{v_x^2 + v_y^2 + v_z^2}$, $F(v)$ is the ion distribution produced with velocity magnitude $v(\geq 0)$ in any direction, and the subscript m represents the mass-to-charge ratio of the MCAI. In the following computations, the subscript m is omitted and is only included for emphasis in certain equations. The TOF profile of the ions is determined by the projection of the velocity distribution $P_m(v_x,v_y,v_z)$ along the x-direction $\tilde{P}_x(v_x)$. We obtain $\tilde{P}_x(v_x)$ by integrating over the two directions perpendicular to the flight axis:

$$P_x(v_x) = \int_{-\infty}^{\infty}\int_{-\infty}^{\infty} P(v_x,v_y,v_z)dv_y dv_z = \int_{v_x}^{\infty} \frac{F(v)}{2v}dv \quad . \tag{S3}$$

The second equality follows from a standard change of variables; we omit the details here. In the experiment, the aperture on the Extractor electrode blocks energetic ions with large off-axis velocities, and only ions that satisfy the following inequality can pass:

$$t_{acceleration1} \cdot \sqrt{v_y^2 + v_z^2} < \Delta \quad . \tag{S4}$$

Equation S4 means that the distance traveled perpendicular to the flight axis in the extraction region must be less than the radius of the aperture. The above inequality implies that for a given value v_x, the maximum total speed (the magnitude of the velocity) of a detected ion should be $U(v_x)$:

$$U(v_x) = \left(v_x^2 + \frac{1}{2}\left(\frac{\Delta}{l_0}\right)^2\left(v_x^2 + a_0 l_0 + v_x\sqrt{v_x^2 + 2a_0 l_0}\right)\right)^{1/2} \quad . \tag{S5}$$

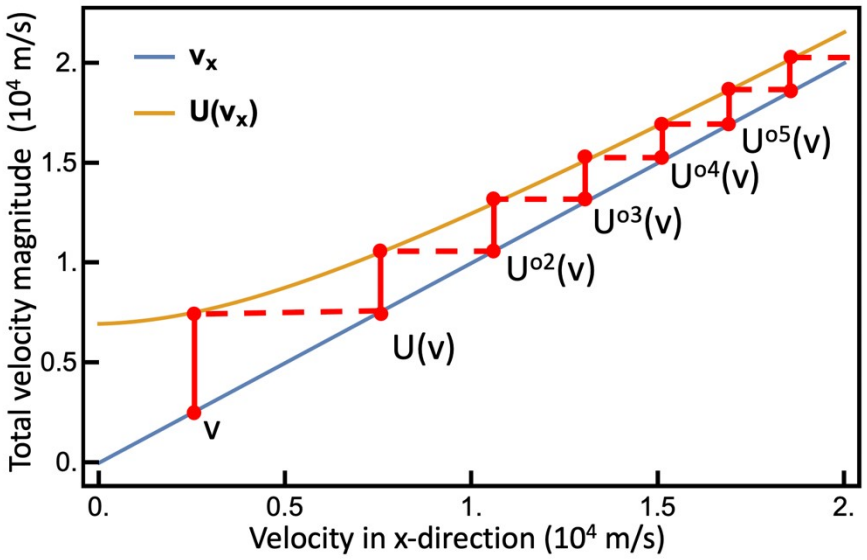

Figure S4: The lower and upper bounds of integration for Eq. S6 are denoted by the blue and yellow curves, respectively, for Ar^{4+}. The red lines depict our strategy to obtain Eq. S15. The vertical red lines depict Eq. S11 for different values of n; the first and second terms on the left side of Eq. S11 are depicted respectively by the bottom and top red dots on the vertical red line. When we sum Eq. S11 for various n's, the terms connected by the horizontal dotted red lines cancel out, leaving only the initial term corresponding to the first red dot when we take the sum of Eq. S11 for $n \geq 0$.

This aperture effect reduces the upper bound of the integration in Eq. S3 to $U(v_x)$, and the values of $U(v)$ are shown in Figure S4. The projection of the velocity distribution in the x-direction for all ions passing through the aperture, $P_x(v_x)$, is thus given as follows:

$$P_x(v_x) = \int_{v_x}^{U(v_x)} \frac{F_m(v)}{2v} dv \quad . \tag{S6}$$

The TOF profile for each charge state, $f_m(t)$, is related to the projected velocity distribution in the *x* direction via a Jacobian factor:

$$f_m(t) = P_x(v_x)\frac{dv_x}{dt} \quad . \tag{S7}$$

2.2 From TOF profile to kinetic energy distribution

From the experimental TOF profile $f_m(t)$, the projected distribution in the *x*-direction $P_x(v_x)$ can be derived via Eq. S7, from which the velocity magnitude distribution $F_m(v)$ can then be obtained based on Eq. S6 using the Fundamental Theorem of Calculus:

$$\frac{dP_x(v_x)}{dv_x} = \frac{U'(v_x)}{2U(v_x)} F_m\big(U(v_x)\big) - \frac{1}{2v_x} F_m(v_x) \quad . \tag{S8}$$

Equation S8 is the same as Eq. 4 in the main text, and since it contains the only variable v_x, we can replace it by v. We solve for $F_m(v)$ from Eq. S8 using a telescopic sum argument. First, we rewrite the equation above as follows

$$F_m(v) - g(v)F_m(U(v)) = -2vP_x'(v) \quad , \tag{S9}$$

with $g(v) = vU'(v)/U(v)$. We then consider this equation evaluated at $U^{\circ n}(v)$, the n^{th} composition of the function U at v, and multiplied by an overall factor of

$$\alpha_n(v) = g(v)g(U(v))\cdots g\left(U^{\circ n-1}(v)\right) = \prod_{k=0}^{n-1} g\left(U^{\circ k}(v)\right) , \quad \text{(S10)}$$

for $n \geq 1$ and $\alpha_0 = 1$. That is, for $n \geq 0$,

$$\alpha_n(v)F_m\left(U^{\circ n}(v)\right) - \alpha_{n+1}(v)F_m\left(U^{\circ n+1}(v)\right) = -2\alpha_n(v)U^{\circ n}(v)P_x'\left(U^{\circ n}(v)\right) , \quad \text{(S11)}$$

where we have set $U^{\circ 0}(v) = v\ by\ convention$. Next, we sum Eq. S11 for $n = 0, 1, \ldots, N$ and obtain

$$F_m(v) - \alpha_{N+1}(v)F_m\left(U^{\circ (N+1)}(v)\right) = -2\sum_{n=0}^{N} \alpha_n(v)U^{\circ n}(v)P_x'\left(U^{\circ n}(v)\right) . \quad \text{(S12)}$$

By taking $N \to \infty$ and for any fixed v, we have $U^{\circ (N+1)}(v) \to \infty$, as shown in Fig. S4, and $F_m\left(U^{\circ (N+1)}(v)\right) \to 0$ since distributions decay to zero at infinity. Additionally, one may show that the terms $\alpha_{N+1}(v)$ are bounded as $N \to \infty$ based on the convergence of Eq. S10, which is satisfied if and only if the following infinite sum converges

$$\sum_{k=0}^{\infty} \left[g\left(U^{\circ k}(v)\right) - 1\right] . \quad \text{(S13)}$$

Using the ratio test, and based on the computed limit from *Mathematica*, we have

$$\lim_{k\to\infty} \left[g\left(U^{\circ (k+1)}(v)\right) - 1\right] / \left[g\left(U^{\circ k}(v)\right) - 1\right] = l_0^2 / \left(l_0^2 + \Delta^2\right) < 1 , \quad \text{(S14)}$$

thereby confirming the convergence of the infinite sum of Eq. S13 and the finite value of $\alpha_{N+1}(v)$ as $N \to \infty$. Then, by taking $N \to \infty$ in Eq. S12, the second term on the left side goes to zero since $F_m\left(U^{\circ (N+1)}(v)\right) \to 0$ and $\alpha_{N+1}(v)$ are bounded. Consequently, we obtain an expression for the distribution of the magnitude of the velocity:

$$F_m(v) = -2\sum_{n=0}^{\infty} \alpha_n(v)U^{\circ n}(v)P_x'\left(U^{\circ n}(v)\right) , \quad \text{(S15)}$$

using $P_x(v_x)$ obtained from the TOF distribution $f_m(t)$ via Eq. S7. In practice, we truncate the summation in Eq. S15 based on the desired level of precision; we discuss this further in the next section (2.3). We may also obtain a formula for the velocity distribution of the energetic ions $P_m(v_x,v_y,v_z)$ via Eq. S2 and Eq. S15.

The kinetic energy distribution $P_m(E_k)$ is related to the velocity magnitude distribution $F_m(v)$ by a Jacobian factor:

$$P_m(E_k) = F_m(v) \times \frac{dv}{dK_e} = -\frac{2}{mv}\sum_{n=0}^{\infty} \alpha_n(v) U^{\circ n}(v) P_x'\left(U^{\circ n}(v)\right) , \quad \text{(S16)}$$

where the second equality is due to Eq. S2.

2.3 Calculation details

The calculation method detailed in the above section is time consuming, particularly when many terms are needed for a high precision. To speed up the calculation, we use a group of Gaussian functions to represent the projected velocity distribution in the *x* direction $P_x(v_x)$:

$$P_x(v_x) = \sum_{k=1}^{d_g} A_k\left(e^{-\frac{(x-\mu_k)^2}{2\sigma_k^2}}\right) \quad \text{(S17)}$$

where A_k is the amplitude, μ_k is the center, σ_k is the width, and d_g is the number of fitting terms, which is typically 3 – 4 terms, depending on a statistical analysis. More terms result in a better representation of the projected velocity distribution, but also result in more time in calculation.

We truncate the number of terms in Eq. S15 for numerical computations

$$F(v) \approx -2\sum_{n=0}^{d_t} \alpha_n(v) U^{\circ n}(v) P_x'\left(U^{\circ n}(v)\right) , \quad \text{(S18)}$$

where d_t depends on the desired level of precision and a physically meaningful result for $F(v)$. When d_t is too small, the calculation can result in a non-physical result in the low velocity region: a negative value for $F(v)$, but when more terms are included, the negative region converges to zero. Thus, one of the lower limits of d_t is the number of terms required to achieve a physically meaningful distribution function. In addition, we also defined a convergence condition to be 0.1% of the difference in velocity between consecutive terms. For example, if the average velocity of Ar^{7+} at d_t = 99 is 1.2874 $\times 10^7$ m/s , and the velocity at d_t = 100 is 1.2881 $\times 10^7 m/s$, we consider the series has converged, and the final velocity is 1.2881 $\times 10^7$ m/s. The higher of the two limits for d_t is used in the calculation.

Furthermore, an analytical expression of the velocity distribution $F(v)$ is crucial in calculating the final kinetic energy distribution, since the Jacobian factor in Eq. S16 would have a singular point as the speed approaches zero if treated numerically. We used a polynomial fit with an exponential decay function to represent the numerator of Eq. S16:

$$F(v) = \sum_{k=1}^{d_s} b_k x^k e^{-x}, \tag{S19}$$

where b_k is the coefficient, and d_s is number of fitting terms.

Interestingly, the resulting velocity magnitude distribution fits well with a Boltzmann-Maxwell distribution:

$$F(v) = A\left(\frac{v}{\sigma}\right)^2 e^{-\frac{1}{2}\left(\frac{v}{\sigma}\right)^2}, \tag{S20}$$

where A is the amplitude, and σ is the width. The σ value of Ar^{4+} can be related to temperature of the ions, which is roughly 200 eV (2.3×10^6 Kelvin) for doped clusters, and 50 eV (5.8×10^5 Kelvin) for neat clusters.

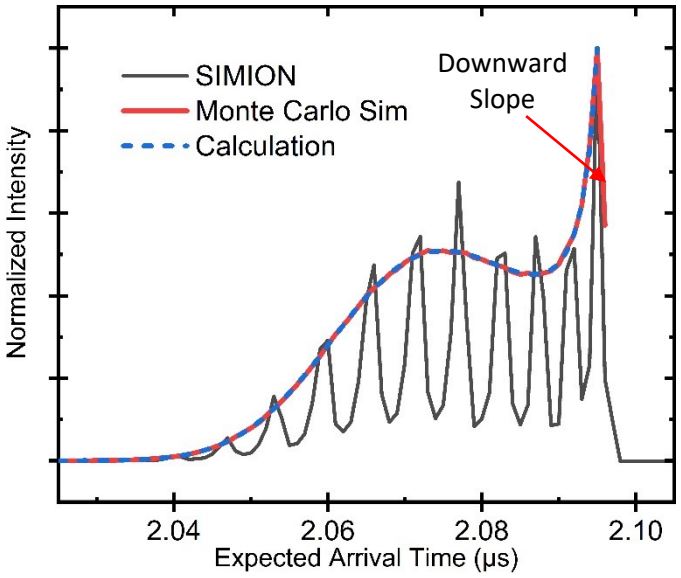

Figure S6: Calculated TOF profiles of Ar^{4+} based on the KE distribution of Fig. S5 using three different methods. The peaks from SIMION simulation are a result of the lensing effect of the aperture on the Extractor electrode. The dashed blue line (calculation) does not contain the downward slope labeled by the red arrow, while both the SIMION and Monte Carol simulations come down in intensity above 2.09 μs.

2.4 Validation of the mathematical approach

We performed a series of Monte-Carlo simulations to validate the above calculations. Using Ar^{4+} as an example, and based on an arbitrary gaussian distribution in kinetic energy shown by the dotted line in Fig. S5, we created a Python code to randomly create ten million ions and calculated their TOF profiles, as shown by the solid red line in Fig. S6. We also used SIMION to generate ten million ions with the same kinetic energy distribution and obtained the TOF profiles as shown by the solid grey line in Fig. S6. The discrete peaks in this simulation are results of the aperture: it behaves like a lens and its lensing effect depends on the KE of the ions, in almost a periodical fashion. These two profiles are in excellent agreement with that produced based on the above equations (dashed blue line in Fig. S6). The downward slope in the TOF profiles from the two Monte-Carlo simulations is a result of the bias in the random number generator function against very low kinetic energies. The solid black line in Figure S5 shows that the retrieved kinetic energy distribution from the derived TOF profile (dashed blue line) using Eq. S18.

To further validate the method, we used the derived $P_m(E_k)$ based on the results from Fig. 3 and Fig. 5, and calculated the expected TOF profile, again using Ar^{4+} as an example. Figure S7

compares the original experimental TOF profile with the thus derived profiles. The agreement among all three profiles is remarkable, although the calculation from Eq. S1 does not include any effect of stray fields, and the treatment of Eq. S18 does not include any ions reflected from the Kicker electrode.

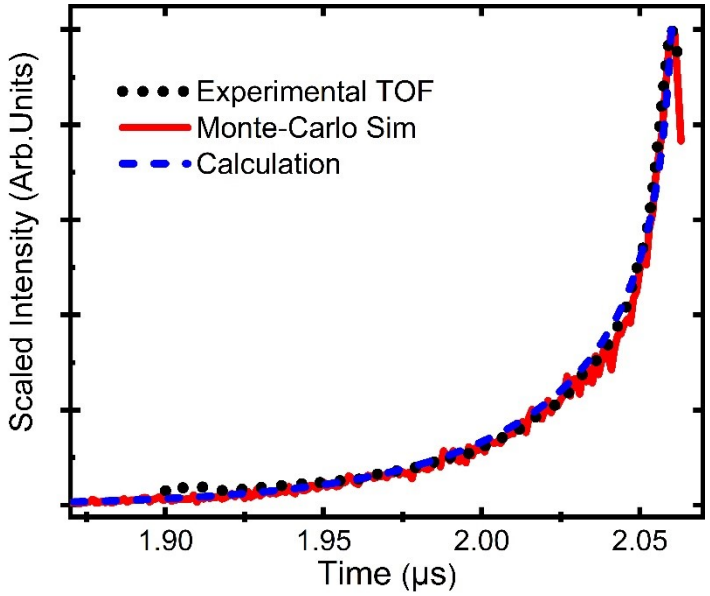

Figure S7: Comparison between the experimental and the derived TOF profiles for Ar^{4+} from $Ar_{800}3ClB_{0.07}$.